Mutual influence between macrospin reversal order and spin-wave dynamics in isolated artificial spin-ice vertices

F. Montoncello, L. Giovannini, Wonbae Bang, J. B. Ketterson, M. B. Jungfleisch, A. Hoffmann, B. W. Farmer, and L. E. De Long

Phys. Rev. B **97**, 014421 — Published 18 January 2018

DOI: 10.1103/PhysRevB.97.014421

Mutual influence between macrospin reversal order and spin wave dynamics in isolated artificial spin ice vertices

F. Montoncello*, L. Giovannini,
Dipartimento di Fisica e Scienze della Terra, Università di Ferrara, Ferrara, ITALY
W. Bang, J. B. Ketterson,
Department of Physics and Astronomy, Northwestern University, Evanston, IL (U.S.A.)
M. B. Jungfleisch, A. Hoffmann
Argonne National Laboratory, Materials Science Division, Argonne, IL (U.S.A)
B.W. Farmer, L.E. De Long
Department of Physics and Astronomy, University of Kentucky, Lexington, KY (U.S.A.)

* *Corresponding Author, email:* montoncello@fe.infn.it

Abstract

We theoretically and experimentally investigate magnetization reversal and associated spin wave dynamics of isolated threefold vertices that constitute a Kagome lattice. The three permalloy macrospins making up the vertex have an elliptical cross section and a uniform thickness. We study the dc magnetization curve and the frequency vs. field curves (dispersions) of those spin wave modes that produce the largest response. We also investigate each macrospin reversal from a dynamic perspective, by performing micromagnetic simulations of the reversal processes, and revealing their relationships to the soft mode profile calculated at the equilibrium state immediately before reversal. The theoretical results are compared with the measured magnetization curves and FMR spectra. The agreement achieved suggests that a much deeper understanding of magnetization reversal and accompanying hysteresis can be achieved by combining theoretical calculations with static and dynamic magnetization experiments.

1. Introduction

Artificial spin ices (ASI), originally conceived to physically emulate atomic spin ices at a mesoscopic scale[1,2,3,4], have recently emerged as an independent topic in the field of magnonics [5,6,7,8,9,10]. An ASI consists of an array of elongated nanomagnets (macrospins) with width, thickness and length dimensions adjusted to promote an approximately uniform magnetization constrained to two "Ising" polarization states (1 and 0) by shape anisotropy. Magnetization reversal, which occurs as a sequence of partial reversals within the ASI, remains incompletely understood, and depends upon underlying symmetries (e.g., periodicity) and defects (e.g., variations of macrospin shape and/or dimensions over the array). Typically, the spatial-temporal sequence of macrospin reversals follows a clear path, and propagates as a "signal" from one edge of the network to another, usually via transitory domain wall (DW) formation and motion.

However, the reversal of individual macrospins can occur by various mechanisms, including uniform rotation of the magnetization as a whole in very small particles where exchange interactions dominate. As the macrospin size increases, reversal can occur via domain wall (DW) nucleation, which can be viewed as an emission of a "+2 magnetic charge" that moves from one end of a nanomagnet to the other [11,12,13]. Alternatively the reversal of a single macrospin is likely to trigger a cascade of reversals through neighboring nanomagnets in an array; such a magnetic charge redistribution can result in the formation of a "Dirac string"[14,15,16,17] consisting of oppositely charged vertices separated by a chain of sequentially reversed segments. The movement

of magnetic charge distributions has potential applications, such as the transport of magnetic beads (or functionalized nanomagnets) trapped in their concomitant stray fields [18].

Regions within an array where macrospins are anti-parallel to the applied field have interesting consequences for the spin wave (SW) dynamics. In those regions, the internal effective field experienced by various spin modes is consistently lower than elsewhere, and, as a result, the lowest frequency modes are localized in those regions [19,20]. Hence, in a given macrospin network, a particular subset of reversed macrospins arising from a given applied field history [21] will display "its own" characteristic SW modes, confined within these reversed macrospins, and with a unique SW frequency spectrum, as a fingerprint of that specific subset at that specific applied field[22]. This "tunability" is particularly attractive for addressing SW excitation/detection issues in spintronic devices [23,24,25,26]. Clearly, the subset of macrospins that will exhibit an inverse magnetization at a given applied field, can act as a tunable path, or waveguide, across the array, which we refer to as an "artificial Dirac string"[27,28,29]. The influence of shape anisotropy on the reversal of macrospin networks has been discussed [30].

In this paper, we will address the relationship between macrospin reversal and the evolution of associated SW frequencies (together with the spatial extent of corresponding modes), in selected, simple systems that can be quantitatively modeled in detail. In particular, we will show how macrospin reversals affect the spin wave frequency and behavior with the applied field, and, in a mutual influence, how "special" spin waves (i.e., the soft modes) affect the macrospin reversal order. The system studied involves isolated vertices formed from three macrospins with long axes oriented 120° relative to each other, a structure that mimics a typical vertex-configuration in periodic Kagome (honeycomb) arrays [2,12,31]. The present study consists of two parts: first, a theoretical study of ideal (regular) systems having standard magnetic parameters; second, an experimental investigation to reveal how the real sample departs from the ideal one, thereby highlighting the more robust behaviors predicted by the calculations.

The theoretical calculations were performed using the dynamical matrix method [32,33], which is based on both the solution of the Hamilton's equations of motion for the spin harmonic precession and a micromagnetic representation of the magnetic system. Each macrospin is modeled as a permalloy dot with an elliptical cross section, with major and minor axis of 500 and 200 nm, and a uniform thickness of 15 nm. This choice was guided by the fact that overly elongated ellipses are known to have low-frequency excitations localized in narrow areas at the ends of the sample (longitudinally), and those modes are unlikely to give strong ferromagnetic resonance (FMR) signals, especially because in real samples imperfections affect the particle edges randomly in the array [34,35,36,37]. Hence, our choice of elliptical macrospins with aspect ratio 2/5 exhibits many low-frequency excitations ("bulk" modes) that occupy most of the dot surface. We performed additional calculations for a three-macrospin-vertex in which one of the ellipses had half the width of the other two (aspect ratio 1/5) to address the effects of shape anisotropy. For all the systems, we investigated the SW dynamics across each macrospin reversal, with special emphasis on those modes with the largest FMR response, since they are most easily detected experimentally and are hence more suitable to carry information in spintronic/magnonic applications. Our theoretical investigation addresses the mode-softening process in some detail.

In the experimental part of the work, we measured DC magnetization curves (at different temperatures) and FMR spectra (room temperature) for samples fabricated to closely mimic the modeled structures.

2. *Modelling an isolated vertex*

We used OOMMF [38] to compute the equilibrium magnetization configuration; as noted, each macrospin consists of a 15-nm-thick-dot with elliptical cross section, 500-nm major axis, 200-nm minor axis (Fig. 1). The simulations considered macrospins constructed from $5\times5\times15$ nm^3 micromagnetic cells ("pixels"). One of three macrospins was assumed to be aligned with an applied magnetic field directed along the x-axis, and the two additional macrospins were symmetrically rotated away from the **x**-axis by ± 120°. A second sample type (Fig. 1-b) was fabricated with a narrower, 100-nm, minor axis for one of the 120° ellipses. The magnetic moment of each macrospin is about $1.0\times10^8\ \mu_B$ (where μ_B denotes a Bohr magneton), while that of the thinner one is about $0.6 \times 10^8\ \mu_B$. The magnetic parameters utilized for Permalloy are: saturation magnetization $M_s = 860$ kA/m, and exchange stiffness parameter $A = 1.3 \times 10^{-11}$ J/m.

For each applied field, we used the equilibrium magnetization texture generated by OOMMF as input for the dynamical matrix software [32,33], which outputs the frequency and phase profile of all the possible spin modes, with no constraint on their symmetry or amplitude. In what follows, we will plot the real, out-of-plane, **z**-component of each mode, which mainly determines, through a volume integration over the sample, the mode strength for relevant measurement techniques (e.g., FMR[39] and Brillouin light scattering[40]).

3. *Calculated results: static hysteresis loops*

In Fig. 1 we show the hysteresis cycles calculated for the two vertex types: symmetric (a), and asymmetric (b). In general, magnetization reversal in larger macrospins is not an abrupt event, but occurs gradually by partial rotation of the individual magnetic moments of the pixels making up each macrospin. The magnetic moment of each pixel experiences the action of a local effective field H_{eff}, which is the sum of an external field and the internal fields determined by the magnetization configuration, the latter being the sum of the exchange and demagnetizing fields. Since our macro spins have uniform thickness and elliptical cross-section, and therefore are *not* ellipsoids of revolution, this effective field H_{eff} is highly inhomogeneous (even in a uniform external field) and consequently, the reversal of the individual moments within each macrospin is non-uniform and not simultaneous. We show the effective internal field distribution close to each of the reversals in Fig. 2.

3.1 *Symmetric vertex*

We prepare a reference state of the system by applying an external field of 100 mT, to generate an "Ising-saturated" state; i.e., in each element the magnetization is aligned to the macrospin axis (Fig. 2-a), apart from slight misalignment of the magnetic moments closer to the ends, due to shape anisotropy. As the external field is decreased, the magnetization gradually decreases as well, down to the first critical field, $B_{c1} = \mu_0 H_{c1} = -29$ mT, at which both oblique macrospins reverse their magnetization. At this stage, all

three macrospins point into the vertex (a "three-in" configuration), thereby generating the largest possible magnetic charge at that point. In practice, the magnetization of any macrospin is not uniform due to shape anisotropy effects. The joint reversal of both oblique macrospins is of course a consequence of symmetry, so that in real samples, with unavoidable fabrication defects/irregularities, there would be slight differences in their reversal fields.

As the external field approaches $\mu_0 H_{c1} = -29$ mT the individual (i.e., the pixels') magnetic moments in a macrospin undergo a gradual rotation that depends on the position of that magnetic moment at a given applied field, since it is controlled by the local position-dependent effective field it actually experiences. As shown in Fig. 2-c, the "minimum" of the effective field (i.e., the largest negative value) is located near the outer ends of the ellipses, and hence the magnetic moments that rotate first (and the most) lie within that region. This effect is determined by the SW dynamics, in particular by the soft mode phase profile and operation [41], and will be discussed in Section 5.

On decreasing the external field further, the "3-in" configuration holds with little modification to the equilibrium magnetization (in Fig. 1, this corresponds to a "plateau" region), until a second critical field is reached at $\mu_0 H_{c2} = -41.5$ mT. Below this value, the magnetization of the horizontal macrospin undergoes an instability involving the generation of a transitory vortex at the end close to the vertex center The vortex is gradually driven to the other end, and eventually expelled, thereby completing the evolution to the new equilibrium state, i.e., with the magnetization reversed. This reversal, which creates a macrospin parallel to the direction of the applied field, produces a large discontinuity in the magnetization curve $M_H(H)$, Fig. 1. At this point, the three-macrospin vertex is in a reversed Ising state. As shown in Fig. 2, the internal effective field minimum occurs in the region close to the vertex, especially for the horizontal macrospin, but also for the other two macrospins, even if only limited to a small area close to the vertex, where the magnetization is still misaligned with the ellipse axis: in those regions, the magnetic moments are the first to undergo instability, as discussed in Sec. 5, and drive the vertex to a completely reversed Ising-saturated state.

3.2 *Asymmetric vertex*

For the asymmetric vertex, we repeat the procedure followed in the previous section, starting from an "Ising-saturated state", at 100 mT (Fig. 2-b). In this system, the broken mirror symmetry with respect to the x-axis results in a different value of the reversal field for each of the oblique macrospins. Note that even though the macrospin with the lower aspect ratio has an average magnetic moment only 0.6 times that of the other two, its reversal is retarded by the stronger dipolar fields arising from its larger shape anisotropy (smaller width). As is apparent in Fig. 1 (dashed line), the upper right macrospin reverses first beyond the critical field $\mu_0 H_{c1} = -29$ mT, followed by the horizontal macrospin at $\mu_0 H_{c2} = -34.5$ mT; the narrow macrospin reverses last at $\mu_0 H_{c3} = -77$ mT (a counterclockwise reversal order).

Similar to the symmetric case, the mechanisms of reversal are moment rotation for the oblique macrospins, and vortex generation for the horizontal one. As shown in Fig. 2,

the areas corresponding to the minima of the effective internal field correspond to the regions where magnetic moments rotate first. The specific mechanism of reversal for each macrospin will be discussed in Sec. 5. As apparent from Fig. 1 (dashed line), the first reversal is characterized by a small discontinuity in the magnetization curve $M_H(H)$ followed by a small "plateau" where the variation of the magnetization is small, and the vertex maintains a "2-in-1-out" configuration. A large discontinuity in the M_H curve occurs next, corresponding to the reversal of the horizontal macrospin, followed by a larger plateau (the magnetization curve varies less dramatically), corresponding to the "1-in-2-out" configuration, where only the thinner macrospin is still not reversed; it persists longer (in terms of applied reverse field) because of the larger shape anisotropy of the thinner macrospin. Finally, the thinner macrospin undergoes reversal, but causes only a small magnetization discontinuity due to its size and inclination with respect to the applied field.

3.3 Conclusions

These above results show how shape anisotropy can alter the order of macrospin reversal, which is particularly important for understanding the sequence of reversals of adjacent macrospins (i.e., for a "Dirac string") in macrospin networks. In the case of atomic spin ices, the string path has a near-random direction; but in magnonics, where ASI are specifically designed for magnonic/spintronic applications, the path of a particular Dirac string can be engineered by tailoring the shape anisotropy, and thereby made to mimic wires in ordinary electronics and information delivery systems.

4. Calculated results: spin wave dynamics

4.1 Symmetric sample

If the magnetization of a system is approximately uniform and aligned with the applied field, one can observe a fundamental mode that is reminiscent of the uniform Kittel mode predicted for saturated ellipsoids. For the three-macrospin vertices under discussion here, the magnetization is generally quite far from being uniformly polarized along the applied field, and, correspondingly, the effective internal field is also quite far from uniform. Hence, the analogue of the fundamental mode is not uniform, but splits into additional modes with similar features, and amplitude localized in different regions of the system where the internal field has different average values (Fig. 2-c,d) and is slowly varying [[42]]. We plot the frequency as a function of the applied field for some principal modes (those likely to give large FMR signals) of a symmetric, threefold vertex in Fig. 3; the corresponding spatial profiles are shown in the insets. The mode expected to have the strongest absorption, and which also has the lowest frequency, is localized within the two oblique macrospins (Fig. 3-a). As shown by the red line in Fig. 3, this mode softens at the first reversal field ($\mu_0 H_{c1}$). The mode expected to have the next largest strength (Fig. 3-c) is localized within the horizontal macrospin, and exhibits a higher frequency. Another volume mode, which should also give a large FMR signal, has two nodal lines orthogonal to the local magnetization direction, and is localized in

the horizontal macrospin (Fig. 3-b). Finally, we show the soft mode that triggers the second reversal at $\mu_0 H_{c2}$ (Fig. 3-d).

We now discuss the spin wave dynamics within three different regimes that are separated by the two critical fields lying in the reversal regime (Fig. 1).

4.1.1 *First regime* (from $\mu_0 H$ = 100 mT to $\mu_0 H_{c1}$= –29 mT). In this field region, where the applied field is being decreased from 100 mT, the magnetization is initially in the Ising-saturated state (Fig. 2-a). As apparent from Fig. 3, the (nodeless) fundamental mode that is localized in the oblique macrospins (bold straight line) has a frequency that decreases with decreasing applied field (apart from a region where, due to the coherent rotation of its inner magnetic moments, the frequency slightly increases), ultimately crossing all the other modes, after which the frequency rapidly goes to zero as the external field approaches $\mu_0 H_{c1}$. This mode has the largest strength at high fields, but loses intensity on approaching $\mu_0 H_{c1}$. This is a characteristic of all soft modes, as will be discussed in the next section. At a somewhat higher frequency, we find the "backward volume mode" with (almost) two nodal lines, leading to weaker absorption for a locally uniform excitation field. Finally, at even higher frequency, we find the fundamental mode localized in the horizontal macrospin: the profile that we calculate is hybridized with a backward volume mode with 6 nodal lines, which lies very close in frequency. Its field behavior is quite simple: a continuous linear decrease down to $\mu_0 H_{c1}$, where it undergoes a slight discontinuity.

4.1.2 *Second regime* – This is a narrow region (spanning from B_{c1} = –29 mT to B_{c2} = –41.5 mT) wherein the magnetization of the two oblique macrospins has reversed, while the horizontal macrospin has not (yielding a "three-in" vertex configuration). Due its antiparallel configuration, we find the minimum of the internal effective field is located in the horizontal macrospin (see Fig. 2-b), and consequently the lowest frequency modes occur here. As is apparent from Fig. 3, the only mode with non-vanishing strength is the fundamental mode of the horizontal macrospin. The lowest frequency mode is shown in Fig. 3-d, which is the soft mode associated with the second transition, as discussed in the next section.

4.1.3 *Third regime* – This regime (B < –41.5 mT) is by symmetry exactly equivalent to the first one, only rotated by 180 degrees and hence will not be discussed.

4.2 Asymmetric sample

For the asymmetric vertex, the effective internal field is again nonuniform, and (independently of the applied field) shows three different average values in the three macrospins (Fig. 2-e,f,g): hence we expect that the ideal Kittel mode is split here into three similar modes, each one at a different frequency, determined by the average

internal field value of the macrospin in which it is confined. The behavior of the mode frequencies with decreasing applied field for the asymmetric vertex is shown in Fig. 4, starting from the Ising-saturated state at high fields. We again have different regimes, depending on which macrospin is reversed. With reference to Fig. 1 inset b), the order of reversal is counterclockwise.

4.2.1 *First regime* – (from 100 mT to –29 mT) In this field region, three modes are expected to yield strong absorption, corresponding to the fundamental modes of each macrospin (Fig. 4-a,b,c): even though localized in nearly identical areas, mode a) has a frequency lower than mode b) because the local magnetization is tilted with respect to the applied field direction, and consequently there is a larger (negative) demagnetizing field, which in turn decreases H_{eff} and hence the mode frequency; on the other hand, mode c) has the largest frequency because, even though the local magnetization is tilted with respect to the applied field direction (in common with mode a), it is confined in a narrower region, with smaller demagnetizing fields along the direction of the magnetization; finally, we note that the amplitudes all three of these modes are hybridized with backward-like volume modes. In addition to these modes, there is a localized mode with much lower amplitude (Fig. 4-d), which is nevertheless important since it becomes the soft mode at the critical field $B_{c1}=-29$ mT (i.e., at the edge of the first macrospin reversal). Note that the frequency-field curves of the b) and c) modes are quite linear, following a Zeeman behavior (though with different slopes), since the magnetization of the corresponding macrospins is essentially unchanged in that field range.

4.2.2 *Second regime* – (ranging from –29 mT to –34.5 mT) We note that the magnetization map of the upper-right macrospin shown in Fig. 2-e, must be interpreted as an "averaged texture", since (due to the chosen shape) a residual curled magnetization persists at the macrospin end close to the vertex. Due to this nonuniform magnetization, the rather uniform mode a) is not found in this regime, while a new nodeless mode arises (Fig. 4-e), which is mainly localized at the right end of the horizontal macrospin, but with important structure visible in the upper-right macrospin: this hybridization is reminiscent of mode a) that survives in such a curled magnetization texure. Also note that modes b) and c) undergo a negligible discontinuity across the first macrospin reversal field because the macrospins supporting these modes are not affected by the transition. Mode a) lies at much higher frequencies (not shown), while mode e) is the new soft mode. At a field slightly larger than $B_{c2}=-34.5$ mT, mode e) triggers an instability that generates a transient vortex and, after its expulsion, the reversal of the entire horizontal macrospin. Note that in this regime, theory predicts only low-intensity modes (i.e., hardly detectable) localized in the thin macrospin, a soft mode, and mode b) in the horizontal macrospin, which has an undulated dynamic magnetization.

4.2.3 Third regime – In this field interval (ranging from –34.5 mT to –75.8 mT), the magnetizations of the two large macrospins are reversed, while that of the thinner macrospin remains in its initial direction. Modes a) and b) now belong to relatively stable macrospins since they experience a decreasing demagnetizing field with increasing (negative) field; hence their frequencies increase almost linearly. Moreover, mode d), missing in the second regime, now reappears, and its frequency increases for the same above reason. Conversely, modes c) and f), which have different locations within the macrospin but are otherwise rather similar [43], belong to a macrospin that is becoming more and more unstable, and hence have frequencies that rapidly decrease and cross other modes: in particular, at the applied field B =–50 mT, modes a) and c) cross at the frequency 8.2 GHz, and hence at this point, both oblique macrospins are simultaneously involved in the magnetic oscillation of the corresponding fundamental modes (shown in the figure insets). At a field slightly larger than the critical field B_{c3} =–75.8 mT, mode f) becomes soft and triggers the reversal of the corresponding macrospin.

4.2.4 Fourth regime – Below –75.8 mT, the magnetization reversal is completed for all the macrospins, hence this regime is by symmetry exactly equivalent to the first one, only rotated by 180 degrees.

5. Spin wave softening and macrospin reversal

In the linear picture of mode dynamics, whenever a discontinuity is present in the magnetization curve, or in its first derivative, a specific mode (among the many in the full spectrum) belonging to some equilibrium texture of the magnetization, becomes "a soft mode"[44,45]. This means that its frequency goes to zero as the applied field approaches a critical transition field value. Since the restoring torque is proportional to the frequency, at the critical field no restoring torque is acting to limit that specific oscillation. The symmetry of this soft mode oscillation then determines the generalized "direction" in which the system initially "moves" during the transition. However, the evolution into high amplitude oscillation necessarily involves nonlinear dynamics, and hence lies outside the framework of any linear, Hamiltonian-based calculation. However, by adiabatic continuation, the initial modifications of the static magnetization are definitely determined by the soft mode symmetry, and this is demonstrated by any simulation tool that traces the early stages of the time evolution of the magnetization texture, when a magnetic field beyond the critical value is applied. Since the soft mode is a low-frequency excitation close to transition, it must be localized at the minima of the effective internal field map $H_{eff} = H_{eff}(x,y)$, which is the sum of the Zeeman, demagnetizing and exchange fields. Depending on the magnetic system's aspect ratio, shape, and various magnetic parameters, the soft modes can have non-zero amplitude in an extended or

restricted fraction of the total system surface [46,47], and correspondingly, they are addressed as bulk or localized soft modes.

We performed OOMMF simulations to verify the theoretical picture presented above. We first constructed an equilibrium magnetization $\mathbf{M}(H;t_0)$ for H just before an instability (t_0 is a given arbitrarily large time). We then incremented the field to H+ϵ (i.e, after instability), and took a snapshot at time $\mathbf{M}(H+\epsilon;t_0+\partial t)$ of the early stages of the non-linear, non-equilibrium evolution of the system. Continuing the simulation for much longer, the new equilibrium magnetization at H+ϵ, $\mathbf{M}(H+\epsilon;\infty)$ ultimately emerges. For all the cases, the field increment ϵ was arbitrarily set to 1 mT. In Fig. 5 we show the results of these simulations for all 5 different transitions discussed above (see details in Fig. 5 caption). By comparing the maps $\mathbf{M}(H+\epsilon;t_0+\partial t)$ and $\partial\mathbf{m}(H;t_0)$ of Fig. 5, it is possible to check, case by case, how the soft mode profile, calculated at H, is imprinted onto the quasi-static magnetization thereby determining the early stages of evolution as some incremental increase, $H+\epsilon$, is applied, well before the final new equilibrium configuration is found. We leave it to the reader to verify the above correspondence by checking how the magnetic moments (illustrated by arrows in the figure) move according to the soft mode phase map. Below, we recall a few only general points:

i. The area where the soft mode profile is the most intense will experience the largest magnetization changes at a transition.
ii. Opposite soft mode phases in different regions produce opposite motions of the magnetization in those regions.
iii. The initial instability in $\mathbf{M}(H+\epsilon;t_0+\partial t)$ can have a symmetry or profile completely different from the future equilibrium configuration $\mathbf{M}(H+\epsilon;\infty)$: when the time interval is very large, the above linear picture breaks down, since adiabatic continuation is broken.
iv. Approaching the reversal field, the out-of-plane component $\partial\mathbf{m}_z$ of the soft mode decreases while the in-plane component (transverse to the applied field, i.e., $\partial\mathbf{m}_y$) increases, as a consequence of an increasingly elliptical precession: this is at the origin of the in-plane instability driving the system to transition. A side effect is a decreasing FMR strength (proportional to the square of the z-component), which we actually observed in our measurements.

In concluding this last aspect of our modeling, we again emphasize that fine details of the quasi-static magnetization evolution following an instability can be understood in terms of the profile of the accompanying soft mode, suggesting it may possible to understand and control certain magnetization changes from a dynamic perspective.

6. Experimental studies on arrays of vertex structures

In this section, we describe the preparation of arrays of well separated Kagome-like vertex structures designed to mimic those modeled theoretically, together with our static and dynamic magnetization studies on them, including comparisons with the predictions of the above model.

6.1 Sample fabrication

All samples consisted of square arrays with a 1.88-μm lattice constant of three-lobed macrospins meeting at a vertex that were patterned in permalloy ($Ni_{80}Fe_{20}$). The symmetric samples had a nominal thickness of 20 nm, but rather than the targeted 200 nm and 500 nm minor and major axis dimensions of the larger elliptical lobes the resulting patterned dimensions were 460 ± 12 nm and 177 ± 7 nm. The thickness of the asymmetric vertices was a nominal 15 nm and the targeted 100 nm narrow lobe of the asymmetric vertex structure was 82 ± 5 nm. The separation between segments at closest approach was 28 ± 3 nm.

Samples used for static magnetization measurements were prepared directly on oxidized Si substrates having a 300-nm-thick SiO_2 layer, while samples made for dynamic studies were prepared on the central strip of a coplanar waveguide (CPW) that was, in turn, patterned on identical substrates. This latter configuration, which involves metallic contact with the guide, has been shown to achieve strong coupling and hence maximal sensitivity[48]. The CPW and the vertex arrays were fabricated using the following process. The conducting electrodes of the CPW were formed with 5-nm layers of Ti covered by 100-nm layers of Au patterned by optical lithography using a laser writer and electron beam evaporation, followed by a lift-off process. The CPW's had a central line flanked by two ground lines; SEM images of a symmetric, and an x-axis aligned, asymmetric vertex are shown in Figs. 6(a) and 6(b). The central line has a 20-micron width, and there was an 8-micron spacing between this line and the two ground lines. The vertex arrays were fabricated by electron beam lithography and electron beam evaporation, using a lift-off process. In order to have a reliable lift-off following metallization, a double layer of positive PMMA was applied using a spin-coater prior to electron beam lithography. The thicknesses of the Ti, Au, and Py films were monitored by a quartz crystal microbalance during the evaporation: deposition rates were ~0.2 Å/sec for Ti, ~1.4 Å/sec for Au, and ~0.4 Å/sec for Py, respectively, and the base pressure was ~3×10^{-7} Torr. The Py for all the samples discussed herein was deposited in a single run. For the static magnetization studies arrays of vertex structures were patterned directly on SiO_2/Si substrates with the same spacing of 1.88 microns over an area of 2 mm x 2 mm.

6.2 DC magnetization loops

6.2.1 Technique and measurement details

Magnetization measurements were performed using a Quantum Design MPMS superconducting quantum interference device (SQUID) that measures the magnetization in an applied field. The samples were diced into approximately 2.5 mm × 2.5 mm squares and attached to the side of a straw using VGE-7031 varnish. They were then loaded into the MPMS with the patterned area approximately centered. The data obtained includes all magnetic contributions; in particular, those arising from the sample, the substrate (silicon in this case), and the varnish (the contribution from the straw is self-canceling). We sweep over a field range that is large enough to saturate the ferromagnetic contribution, which allows us to record the linear diamagnetic response from the substrate and the varnish, which we subtract from the data to obtain the ferromagnetic contribution. We have normalized all data to the saturated ferromagnetic magnetization. The measurements reported here were performed at T = 5 K.

6.2.2 Results and discussion

The $M_H(H)$ experimental curves are shown in Fig. 7 for both the symmetric (black curve) and asymmetric (red curve) samples: we find good agreement with the calculated reversal fields for the first transition. Compared to the theoretical curves of Fig. 1, differences between loop shape, steepness of the magnetization curve in decreasing field, absence of the extension of the magnetization "plateau", and the absolute value of the magnetization discontinuities, can be ascribed to patterning errors in writing individual elements (element size, but also angular displacement) and other inhomogeneities.

6.3 FMR measurement (technique and results)

6.3.1 Technique and measurement details

The FMR experiments employed an external magnetic field constrained to lie along the wave guide axis; hence we report data for only a single static field direction for which the microwave field is largely normal to the static magnetic field. In the SEM image shown in Fig. 6(a) the symmetric vertices are oriented at 0° relative to the guide axis, while Fig. 6(b) shows an image of similarly aligned asymmetric vertices.

In order to probe the dynamic response of the vertices, we performed broadband FMR measurements with a vector network analyzer (VNA)[49]. The VNA is connected via picoprobes to the CPW for recording the microwave absorption spectra, and the transmission parameter S_{21} is measured at a nominal microwave power of –1 dBm. All spectra were recorded using the following routine: First, the dc magnetic field was set at 3000 Oe and the frequency swept between 2 and 12 GHz to establish a baseline (containing non-resonant frequency-dependent responses) which was subtracted from the data gathered at all other fields. Field sweeps were then carried out between +1000 Oe and $-1000\,\mathrm{Oe}$ for discrete frequencies ranging between 2 and 10 GHz. To establish the history dependence of the spectra this procedure was occasionally repeated with the field swept in the range $-1000\,\mathrm{Oe}$ to +1000 Oe.

6.3.2 Results for the symmetric vertex

The FMR spectrum for the sample with the symmetric vertices is shown in Fig. 8 (Panel I and II). In Panel (I) we show dispersion for a slightly thicker sample (nominal 20 nm) than that modeled (15 nm), that shows rather clearly the three main curves of Fig. 3 (with the same corresponding labels a,b,c), showing high FMR intensity, with curve (b), in the middle, having relatively lower intensity; curves a) and b) seem to merge (as in the calculated dispersions) and are detected only down to about –30 mT, while curve c) seems to survive down to –40 mT, in excellent agreement with the calculated values. Unfortunately, in both cases, no signal was detected below 4 GHz, so that mode d) (leading to the second reversal) was not detected.

In Panel (II) we plot the dispersion for the nominal 15 nm symmetric vertex, with identical features and still in good agreement with calculations, but without the presence of curve (b): this effect is due to a lower FMR signal, which decreases the resolution of tiny peaks, and is caused by the reduced amount of magnetic material with respect to the case of 20 nm. While a variation of 5 nm in the calculations would not change the overall picture of the dynamics, but only slightly shift the frequencies, the two results of Panel I and II clearly show how thickness can be critical in determining a better contrast in FMR spectra.

6.3.3 Results for the asymmetric vertex

The FMR spectrum of the asymmetric vertex is shown in Fig. 8-Panel III. We have identified the two main curves as corresponding to modes a) and b), in good agreement with the predictions. However, no evidence was found for mode d), possibly because it is strongly confined within the narrow macrospin, and thus generates a comparatively weaker signal [34,39].

7. Conclusions

In summary, we performed simulations and experiments on the statics and dynamics of symmetric and asymmetric structures consisting of three ellipses of uniform thickness which closely approach each other at a vertex and are oriented at 120°. Particular attention in the simulations was given to the behavior of spin wave modes with the largest intensity, and the behavior of soft modes near macrospin reversals under field sweeps. Our simulations of the reversal process revealed a correspondence between the spatial maps of the soft mode intensity and the early-stage evolution of the quasistatic magnetization texture. In other words, the soft mode profile provides a fingerprint of the magnetization reversal process: fine details of the static magnetization evolution can be understood in terms of the soft mode profile.

Measurements of the static and dynamic magnetic response of the arrays, made of non-interacting vertices, confirmed several of the theoretical predictions, the most interesting of which are:

i. The first reversal consists of a discontinuity **ΔM** followed by a "plateau" over a field interval ΔH, both being substantially larger in the symmetric case (where two large macrospins reverse) than in the asymmetric case (where only a single macrospin reverses). The "plateau" is observed for both vertex types at a low value of magnetization: negative for the symmetric vertex, positive for the asymmetric one. In both cases, the plateau is followed by a large magnetization discontinuity, corresponding to the reversal of the macrospin parallel to the applied field (i.e., to the direction of the plotted magnetization component).
ii. The reversal of the thinner macrospin occurs via a gradual rotation of the magnetic moments, which is a slow process (i.e., occurring within a wider field range): this is actually signaled by another (larger) plateau, at a strongly negative value of magnetization.
iii. The large amplitude modes are the fundamental modes associated to the individual macrospins, with frequencies determined by their internal field, which will be larger for the narrower or horizontal macrospins, and lowest for the oblique macrospins.
iv. The small window with no experimental FMR signal between −25 mT and −35 mT (Fig. 8) is consistent with the calculated results, in that only low intensity modes are predicted in this field interval (see Sec. 4.2.2).

In this work, we have analyzed a single vertex of a typical Kagome lattice, and have focused on the mutual influence between macrospin reversal order and spin wave dynamics: this is a first step in understanding the dynamic behavior of macrospins undergoing reversal in extended networks (periodic lattices), or more complex structures (e.g., artificial quasi-crystals [50]). In particular, on the one hand, we identified how the magnetization reversal of individual macrospins can be

determined, and hence controlled, by the dynamic action of the critical (soft) spin waves. Then, on the other hand, we showed how the single reversal events change both the frequency regime and dependence on the applied field of large amplitude modes: in extended macrospin networks, formed by many of the above vertices, these modes would occur confined in specific regions ("lines") of the network (Dirac strings), depending on the bias field. These regions would mimic the wires common to ordinary electronics, but with a radically improved efficiency due to the action of the dissipation-less spin waves, operating as information delivery carriers in magnon-spintronic devices[51,52].

8. *Acknowledgements*

Work at Northwestern was supported by the NSF under grant DMR 1507058. Work at the University of Kentucky was supported by the NSF under grant DMR 1506979. Work at Argonne was supported by the U.S. Department of Energy, Office of Science, Materials Science and Engineering Division. Use was made of the Center for Nanoscale Materials, an Office of Science user facility, which is supported by DOE, Office of Science, Basic Energy Science under Contract No. DE-AC02-06CH11357.

Figure captions

Figure 1: Hysteresis of the magnetization component M_H parallel to the applied field **H** for the symmetric (solid line) and asymmetric (dashed line) samples normalized to the saturation magnetization M_S. The geometry of the three-lobed vertex structures are shown in insets a) and b).

Figure 2: Equilibrium magnetization configurations at $B=\mu_0 H=50$ mT, referred to as an "Ising saturated state", for the symmetric (a) and asymmetric (b) vertices. Internal effective field maps (component parallel to the applied field) at (c) B = –28.3 mT; (d) B = –41.5 mT; (e) B = –29 mT; (f) B = –34 mT; (g) B = –75.8 mT. Note that deep blue (–1, in arbitrary units)) refers to minima (i.e., the maximum misalignment of **M** with **H**). **H**, in the figure, is directed to the left.

Figure 3: Frequency of the largest power spin wave modes as a function of applied field (decreasing from 100 mT), and (insets on the right) corresponding profiles (real, out-of-plane component of the

dynamic magnetization). Bold red line, labeled a) is the first fundamental mode, going soft at B_{c1} = –28.3 mT; b) is a backward-volume-like mode, c) second fundamental mode (though highly hybridized), d) is the soft mode at B_{c2} = –41.5 mT. Profiles a), b), c) were calculated at 100 mT, and profile d) (which was magnified 300%) at – 41.5 mT.

Figure 4: Frequency vs. applied field curves for the main modes discussed in the text. Modes a-c are the fundamental modes of each macrospin, while d-f are the soft modes at the corresponding transition fields: B_{c1}=–29 mT, B_{c2}=–34 mT, B_{c3}=–75.8 mT. The insets a) to f) are real z-components of the dynamic magnetization of the spin wave modes discussed in the text. Modes a), b) and c) were calculated at H = 50 mT, while mode d) at –29 mT, mode e) at –34 mT, mode f) at –75.8 mT. In insets d-f, the amplitude has been magnified three times with respect to a) to c).

Figure 5: Illustration of the triggering mechanism by which the soft mode initiates instabilities in the symmetric (a,b) and asymmetric (c,d,e) vertices. (a) H = –28.3 mT; (b) H = –41.5 mT; (c) H = -29 mT; (d) H = –34 mT; (e) H = –75.8 mT. The first column shows the equilibrium magnetization (red/blue color scale is the y component) at applied field H; the second column shows the imaginary y-component of the soft mode at H (rainbow color scale is the phase amplitude); the third column shows a snapshot of the magnetization at an early stage of the simulated reversal process. In the OOMMF simulations of reversal, the field variation ϵ was set to 1 mT for all cases, while the time variation ∂t was set arbitrarily close to the starting point, until some evidence of the soft mode profile was apparent. The fourth column shows the equilibrium ($t\rightarrow \infty$) magnetization at the applied field H+ ϵ.

FIG. 6. SEM images of the two sample types with a spacing of 1.88 μm prepared: (a) is a symmetric sample for which all three lobes have the same aspect ratio; and (b) is an asymmetric sample where the width of one lobe is reduced relative to the other two lobes.

Figure 7: Experimental DC magnetization loops at 5 K, either for the symmetric (black, open triangles) and asymmetric (red, full squares) vertices. The arrow and dashed circle indicate a small magnetization plateau region, corresponding to the predicted region between B_{c1} and B_{c2} of Fig. 1 (dashed line), between the first and second macrospin reversal.

Figure 8. Experimental FMR spectra for (I) symmetric (thickness 20 nm), (II) symmetric (thickness 15 nm), and (III) asymmetric vertices. The arrow shows the direction in which the magnetic field was swept. Note the close correspondence with the calculated results of Figs. 3 and 4 (where the same labels indicate the corresponding measured curves).

REFERENCES

[1] Ian Gilbert, Cristiano Nisoli, and Peter Schiffer, Physics Today 69, 7, 54 (2016); doi: 10.1063/PT.3.3237.

[2] R. F. Wang, C. Nisoli, R. S. Freitas, J. Li, W. McConville, B. J. Cooley, M. S. Lund, N. Samarth, C. Leighton,V. H. Crespi and P. Schiffer, Nature **439**, 303 (2006); doi:10.1038/nature04447.

[3] Rougemaille, F. Montaigne, B. Canals, M. Hehn, H. Riahi, D. Lacour and J.-C. Toussaint, New Journal of Physics **15**, 035026 (2013).

[4] A. Farhan, P. M. Derlet, L. Anghinolfi, A. Kleibert, and L. J. Heyderman, Physical Review B 96, 064409 (2017).

[5] Y. Li, G Gubbiotti, F. Casoli, F. J. T. Gonçalves, S. A. Morley, M. C. Rosamond, E. H. Linfield, C. H. Marrows, S. McVitie and R. L. Stamps, J. Phys. D: Appl. Phys. 50 015003 (2017).

[6] Xue Zhou , Geng-Li Chua , Navab Singh, and Adekunle O. Adeyeye, Adv. Funct. Mater. **26**, 1437 (2016).

[7] Ezio Iacocca, Sebastian Gliga, Robert L. Stamps, and Olle Heinonen, Phys. Rev. B 93, 134420 (2016).

[8] Sebastian Gliga, Attila Kakay, Laura J. Heyderman, Riccardo Hertel, and Olle G. Heinonen, Phys. Rev. B 92, 060413(R) (2015).

[9] Matthias B. Jungfleisch, Wei Zhang, Junjia Ding, Wanjun Jiang, Joseph Sklenar, John E. Pearson, John B. Ketterson, and Axel Hoffmann, Appl. Phys. Lett. 108, 052403 (2016).

[10] M. B. Jungfleisch, W. Zhang, E. Iacocca, J. Sklenar, J. Ding, W. Jiang, S. Zhang, J. E. Pearson, V. Novosad, J. B. Ketterson, O. Heinonen, and A. Hoffmann, Phys. Rev. B 93, 100401 (2016).

[11] P. Mellado, O. Petrova, Y.C. Shen, O. Tchernyshyov, Phys. Rev. Lett. 105 (2010) 187206.

[12] Y.C. Shen, O. Petrova, P. Mellado, S. Daunheimer, J. Cumings, O. Tchernyshyov, New J. Phys. 14 (19) 035022 (2012).

[13] S. Krause, G. Herzog, T. Stapelfeldt, L. Berbil-Bautista, M. Bode, E.Y. Vedmedenko, and R. Wiesendanger, Phys. Rev. Lett. 103, 127202 (2009).

[14] Elena Mengotti, Laura J. Heyderman, Arantxa Fraile Rodríguez, Frithjof Nolting, Remo V. Hügli, and Hans-Benjamin Braun, Nature Physics 7, 68–74 (2011).

[15] C. Castelnovo, R. Moessner, and S. L. Sondhi, Nature 451, 42-45 (2008).

[16] D.J.P. Morris, D.A. Tennant, S.A. Grigera, B. Klemke, C. Castelnovo, R. Moessner, C. Czternasty, M. Meissner, K.C. Rule, J.-U. Hoffmann, K. Kiefer, S. Gerischer, D. Slobinsky, R.S. Perry, Science 326, 411-414 (2009).

[17] Y. Tokiwa, T. Yamashita, M. Udagawa, S. Kittaka, T Sakakibara, D. Terazawa, Y. Shimoyama, T. Terashima, Y. Yasui, T. Shibauchi, and Y. Matsuda, Nature Communications 7, 10807 (2016).

[18]Marco Donolato, Paolo Vavassori, Marco Gobbi, Maria Deryabina, Mikkel F. Hansen, Vitali Metlushko, Bojan Ilic, Matteo Cantoni, Daniela Petti, Stefano Brivio, Riccardo Bertacco, Adv. Mater. 22, 2706 (2010).

[19] G. Gubbiotti, M. Madami, S. Tacchi, G. Carlotti, H. Tanigawa, T. Ono, L. Giovannini, F. Montoncello, and F. Nizzoli, Phys. Rev. Lett. 97, 247203 (2006).
[20] Marco Madami, Federico Montoncello, Giulia Capuzzo, Loris Giovannini, Fabrizio Nizzoli, Gianluca Gubbiotti, Silvia Tacchi, Giovanni Carlotti, Hirobonu Tanigawa, and Teruo Ono, IEEE Trans. Magn. **46**,1531 (2010).
[21] Ian Gilbert, Gia-Wei Chern, Bryce Fore, Yuyang Lao, Sheng Zhang, Cristiano Nisoli, Peter Schiffer, Phys. Rev. B 92, 104417 (2015).
[22] Sebastian Gliga, Attila Kákay, Riccardo Hertel, and Olle G. Heinonen, Phys. Rev. Lett. 110, 117205 (2013).
[23] L.J. Heyderman, R.L. Stamps, J. Phys.: Condens. Matter 25, 363201 (2013).
[24] Robert L. Stamps, Stephan Breitkreutz, Johan Åkerman, Andrii V. Chumak, YoshiChika Otani, Gerrit E. W. Bauer, Jan-Ulrich Thiele, Martin Bowen, Sara A. Majetich, Mathias Kläui, Ioan Lucian Prejbeanu, J. Phys. D: Appl. Phys. 47, 333001 (2014).
[25] F. Montoncello, L. Giovannini, Appl. Phys. Lett. 104, 242407 (2014).
[26] F. Montoncello, L. Giovannini, Advances in Materials Science and Engineering, Volume 2016, Article ID 4243817 (2016), http://dx.doi.org/10.1155/2016/4243817.
[27] Y. Perrin, B. Canals, and N. Rougemaille, Nature 540, 410-413 (2016).
[28] S. Ladak, D. E. Read, G. K. Perkins, L. F. Cohen, and W. R. Branford, Nature Physics 6, 359-363 (2010).
[29] Jason P. Morgan, Aaron Stein, Sean Langridge, and Christopher H. Marrows, Nature Physics 7, 75–79 (2011).
[30] R. V. Hügli, G. Duff, B. O'Conchuir, E. Mengotti, A. Fraile Rodríguez, F. Nolting, L. J. Heyderman and H. B. Braun, *Phil. Trans. R. Soc. A* (2012) **370**, 5767–5782.
[31] Jasper Drisko, Stephen Daunheimer, and John Cumings, Phys. Rev. B 91, 224406 (2015).
[32] M. Grimsditch, L. Giovannini, F. Montoncello, F. Nizzoli, G. K. Leaf, and H. G. Kaper, Phys. Rev. B 70, 054409 (2004).
[33] L. Giovannini, F. Montoncello, F. Nizzoli, Phys. Rev. B **75**, 024416 (2007).
[34] Matthias B. Jungfleisch, Joseph Sklenar, Junjia Ding, Jungsik Park, John E. Pearson, Valentine Novosad, Peter Schiffer, and Axel Hoffmann. Phys. Rev. Applied 8, 064026 (2017).
[35] G. Gubbiotti, M. Madami, S. Tacchi, G. Carlotti and T. Okuno, Phys. Rev. B 73, 144430 (2006).
[36] S.O. Demokritov B. Hillebrands , A. N. Slavin, Physics Reports **348**, 441 (2001).
[37] C. Bayer, J. Jorzick, B. Hillebrands, S. O. Demokritov, R. Kouba, R. Bozinoski, A. N. Slavin, K. Y. Guslienko, D. V. Berkov, N. L. Gorn, M. P. Kostylev, Phys. Rev. B 72, 064427 (2005).
[38] M. Donahue, D. G. Porter, Object oriented micromagnetic framework (OOMMF) User's Guide, Version 1.0, Interagency Report NISTIR 6376 (NIST, Gaithersburg, MD, USA, 1999).
[39] M. Mruczkiewicz, M. Krawczyk, R. V. Mikhaylovskiy and V. V. Kruglyak, Phys. Rev. B 86, 024425 (2012).
[40] G. Gubbiotti, G. Carlotti, T. Okuno, M. Grimsditch, L. Giovannini, F. Montoncello, and F. Nizzoli, Phys. Rev. B 72, 184419 (2005).
[41] F. Montoncello, L. Giovannini, B. Farmer, L. De Long, Journal of Magnetism and Magnetic Materials 423, 158 (2017).
[42] F. Montoncello and F. Nizzoli, Journal of Applied Physics 107, 023906 (2010).
[43] Although mode f) is rather localized and has no nodal lines, whereas there is clear undulation in mode c).
[44] L. D. Landau, E. M. Lifshitz, et al. Statistical Physics: Volume 5 (Course of Theoretical Physics), 3rd edition, Butterworth-Heinemann, Oxford, Boston, Johannesburg, Melbourn, New Delhi, Singapore, 1980.
[45] F. Montoncello, L. Giovannini, F. Nizzoli, P. Vavassori, M. Grimsditch, Phys. Rev. B 77, 214402 (2008).

[46] F. Montoncello, L. Giovannini, F. Nizzoli, H. Tanigawa, T. Ono, G. Gubbiotti, M. Madami, S. Tacchi, G. Carlotti, Phys. Rev. B 78, 104421 (2008).
[47] X. F. Han, M. Grimsditch, J. Meersschaut, A. Hoffmann, Y. Ji, J. Sort, J. Nogués, R. Divan, J. E. Pearson, and D. J. Keavney Phys. Rev. Lett. 98, 147202 (2007).
[48] V. Novosad, F. Y. Fradin, P. E. Roy, K. S. Buchanan, K. Yu. Guslienko, and S. D. Bader, Phys. Rev. B 72, 024455 (2005).
[49] S.S. Kalarickal, P. Krivosik, M. Wu, C.E. Patton, M.L. Schneider, P. Kabos, T.J. Silva, and J.P. Nibarger, J. Appl. Phys. 99, 093909 (2006).
[50] V.S. Bhat, J. Sklenar, B. Farmer, J. Woods, J.T. Hastings, S.J. Lee, J.B. Ketterson, L.E. De Long, Phys. Rev. Lett. 111, 077201 (2013).
[51] A. V. Chumak, V. I. Vasyuchka, A. A. Serga, B. Hillebrands, Nature Physics 11, 453 (2015).
[52] A. V. Chumak, A. A. Serga, B. Hillebrands J. Phys. D: Appl. Phys. 50, 244001 (2017).

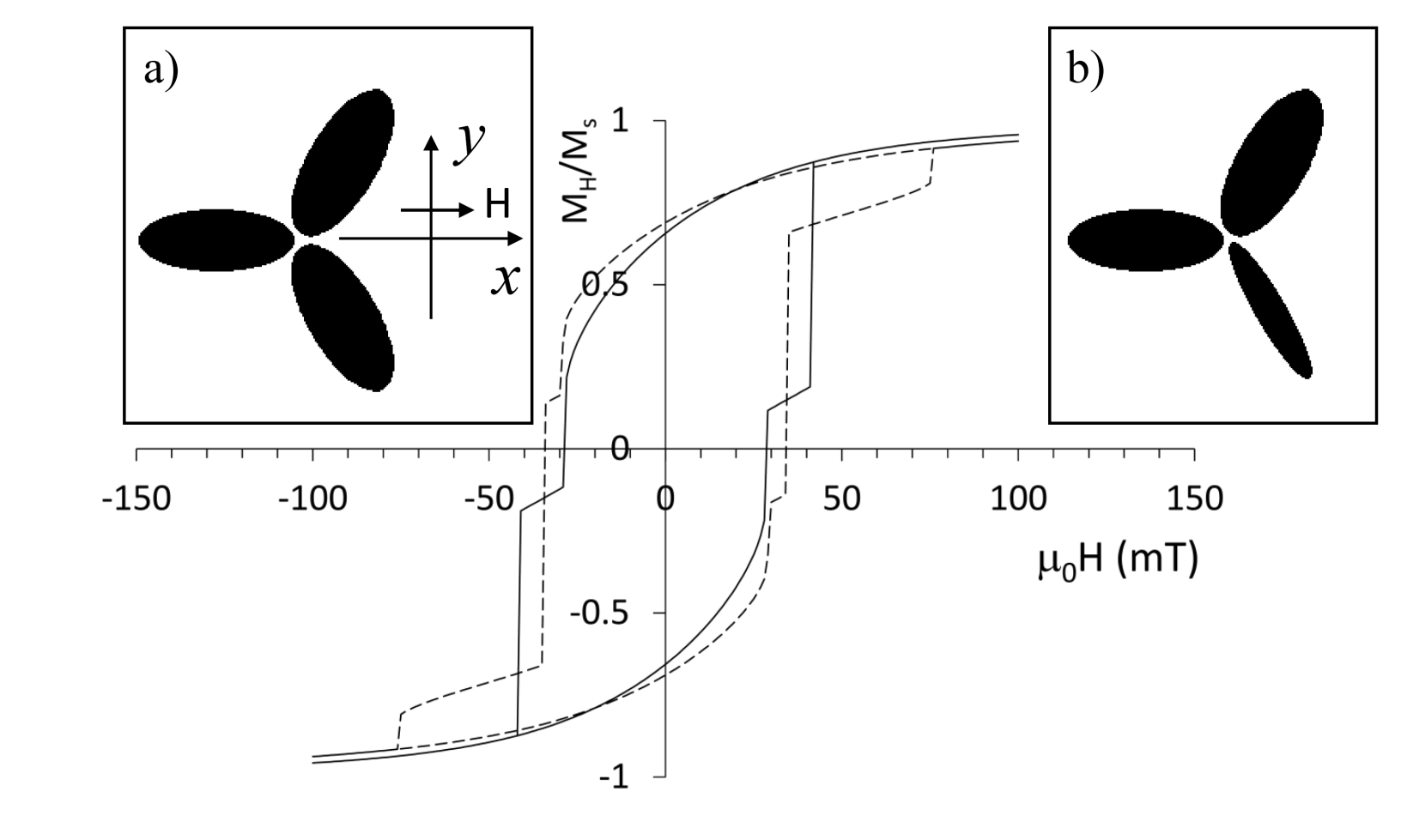
a)
y
H
x
b)
M_H/M_s
1
0.5
0
-0.5
-1
-150
-100
-50
0
50
100
150
$\mu_0 H$ (mT)

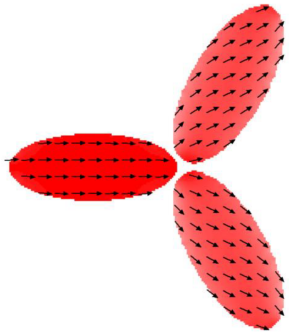

(a)

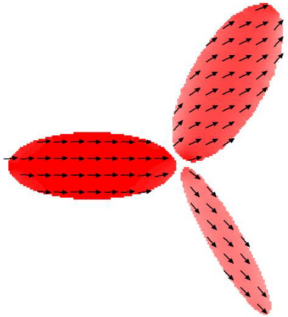

(b)

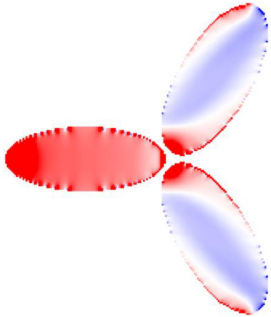

(c)

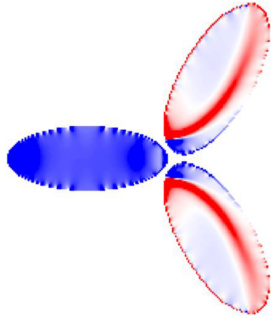

(d)

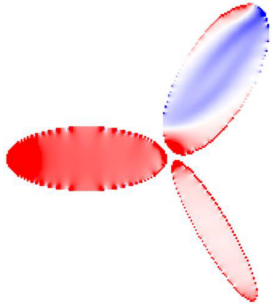

(e)

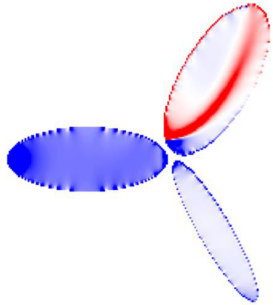

(f)

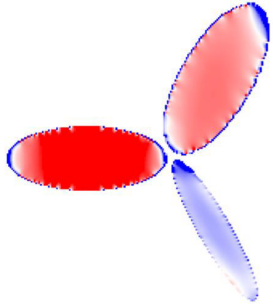

(g)

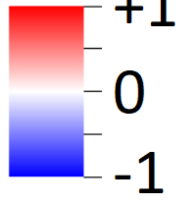

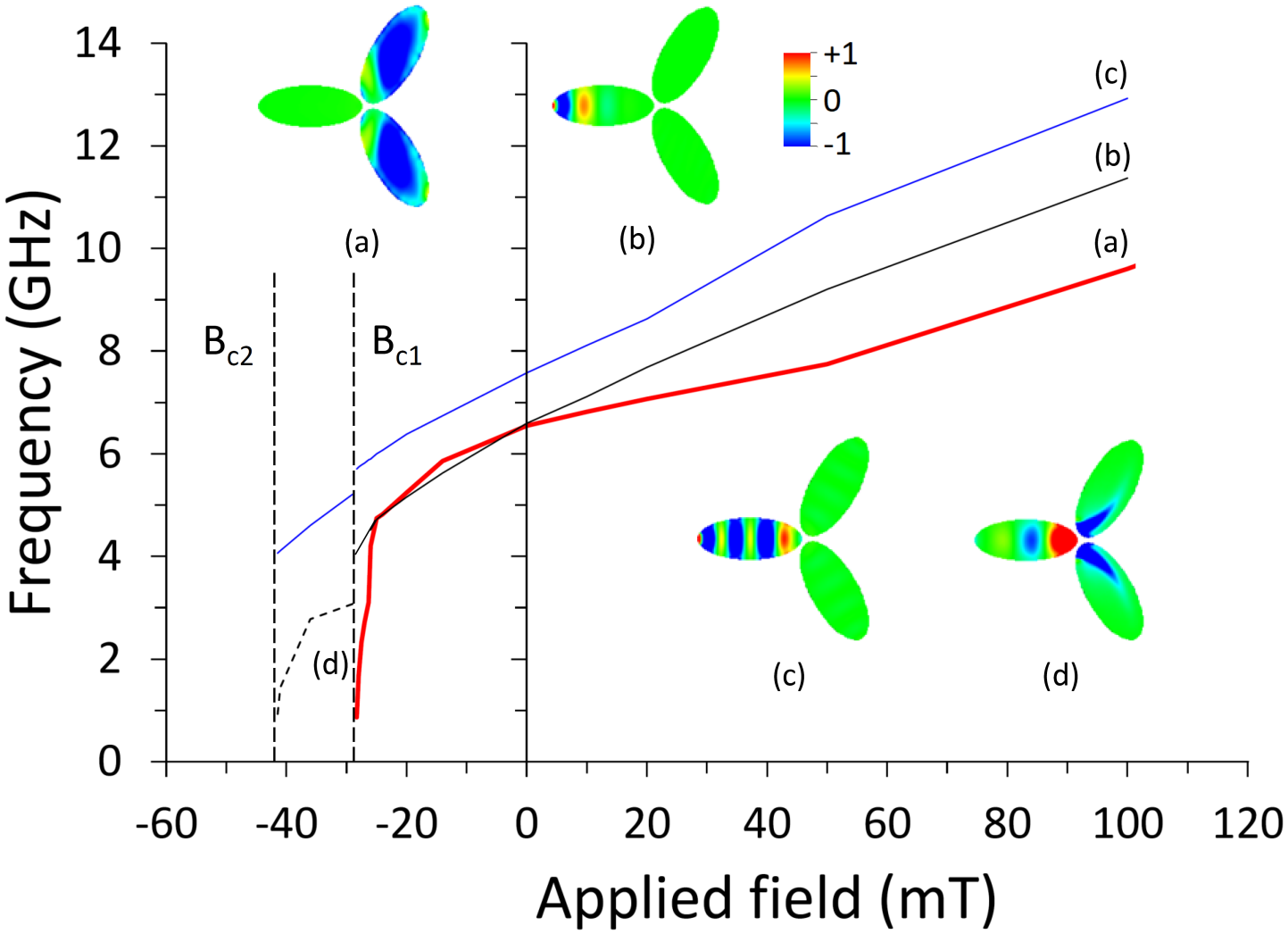
Frequency (GHz)
Applied field (mT)
B$_{c2}$
B$_{c1}$
(a)
(b)
(c)
(d)
+1
0
-1

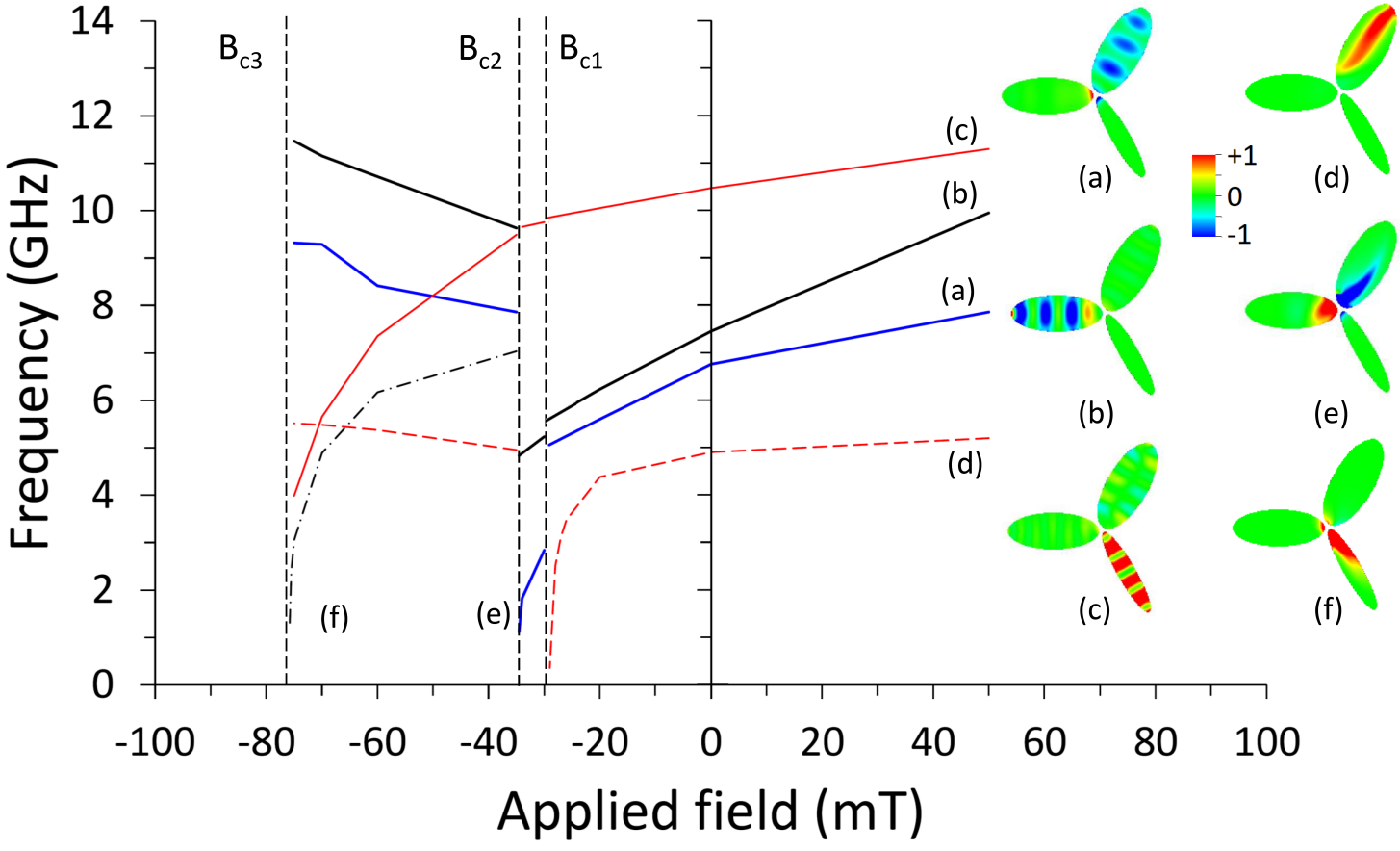
Frequency (GHz)
Applied field (mT)
B_{c3}
B_{c2}
B_{c1}
(a)
(b)
(c)
(d)
(e)
(f)
+1
0
-1

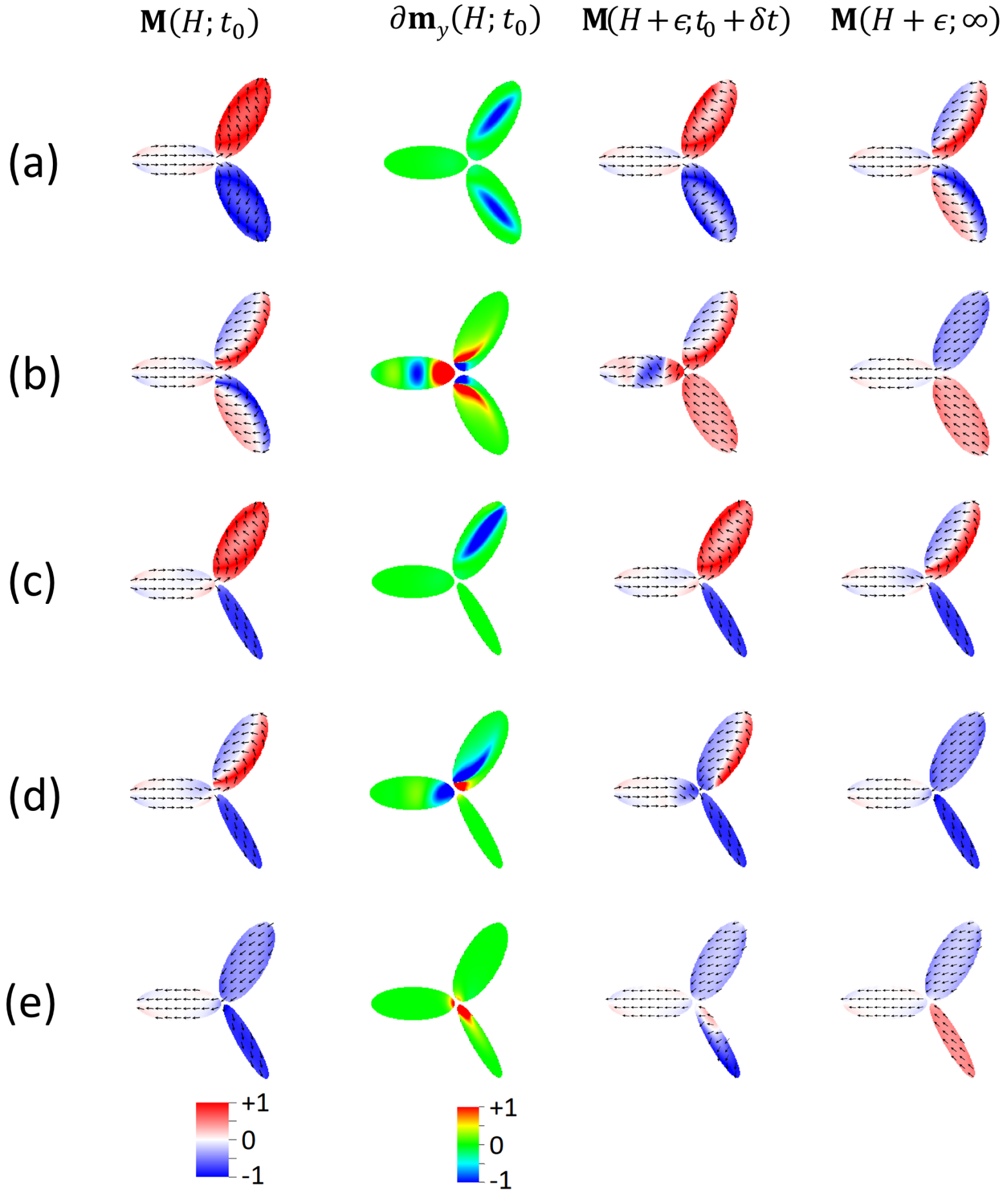
$\mathbf{M}(H;t_0)$
$\partial\mathbf{m}_y(H;t_0)$
$\mathbf{M}(H+\epsilon;t_0+\delta t)$
$\mathbf{M}(H+\epsilon;\infty)$
(a)
(b)
(c)
(d)
(e)
+1
0
-1
+1
0
-1

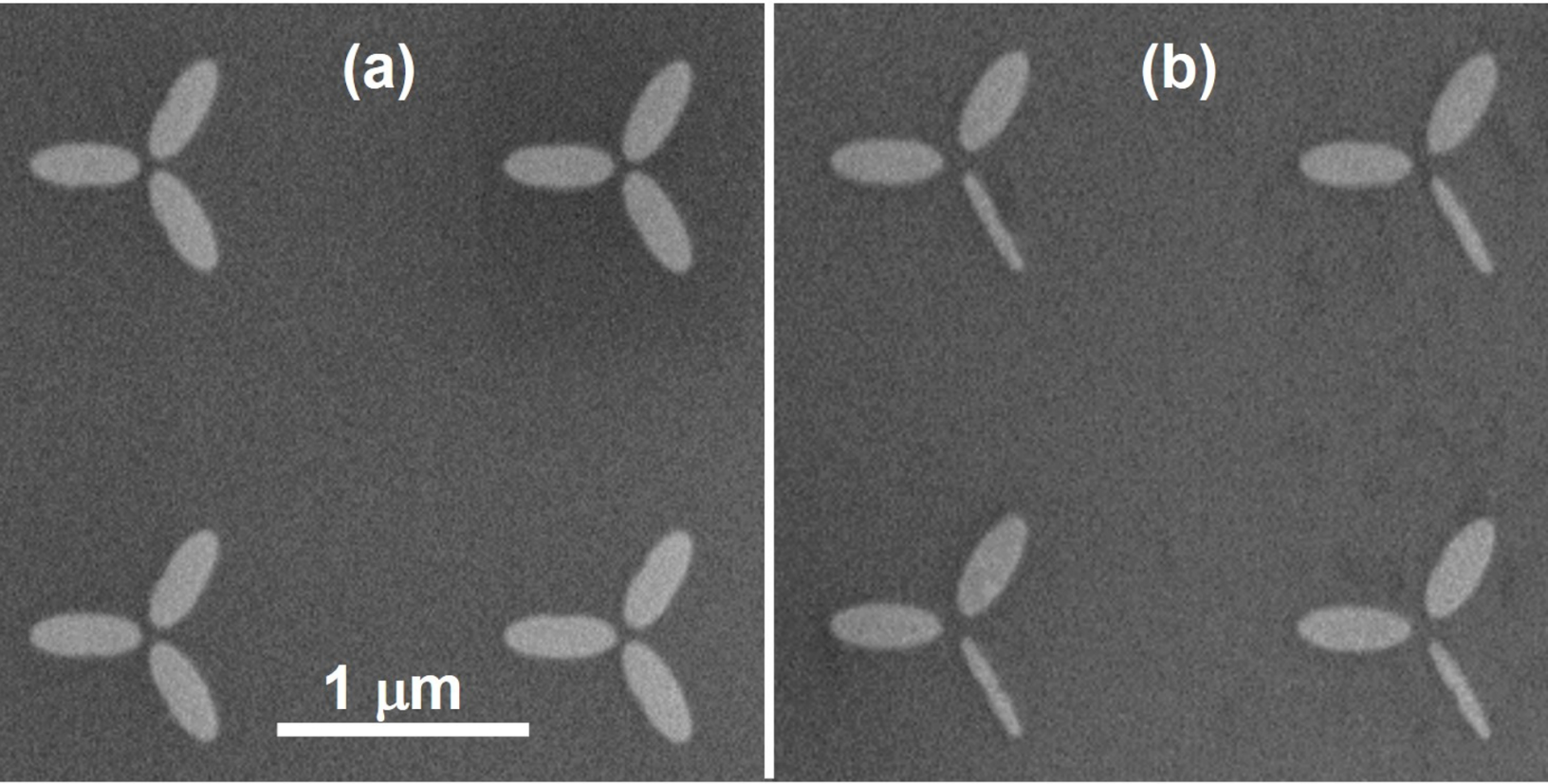
(a)
(b)
1 μm

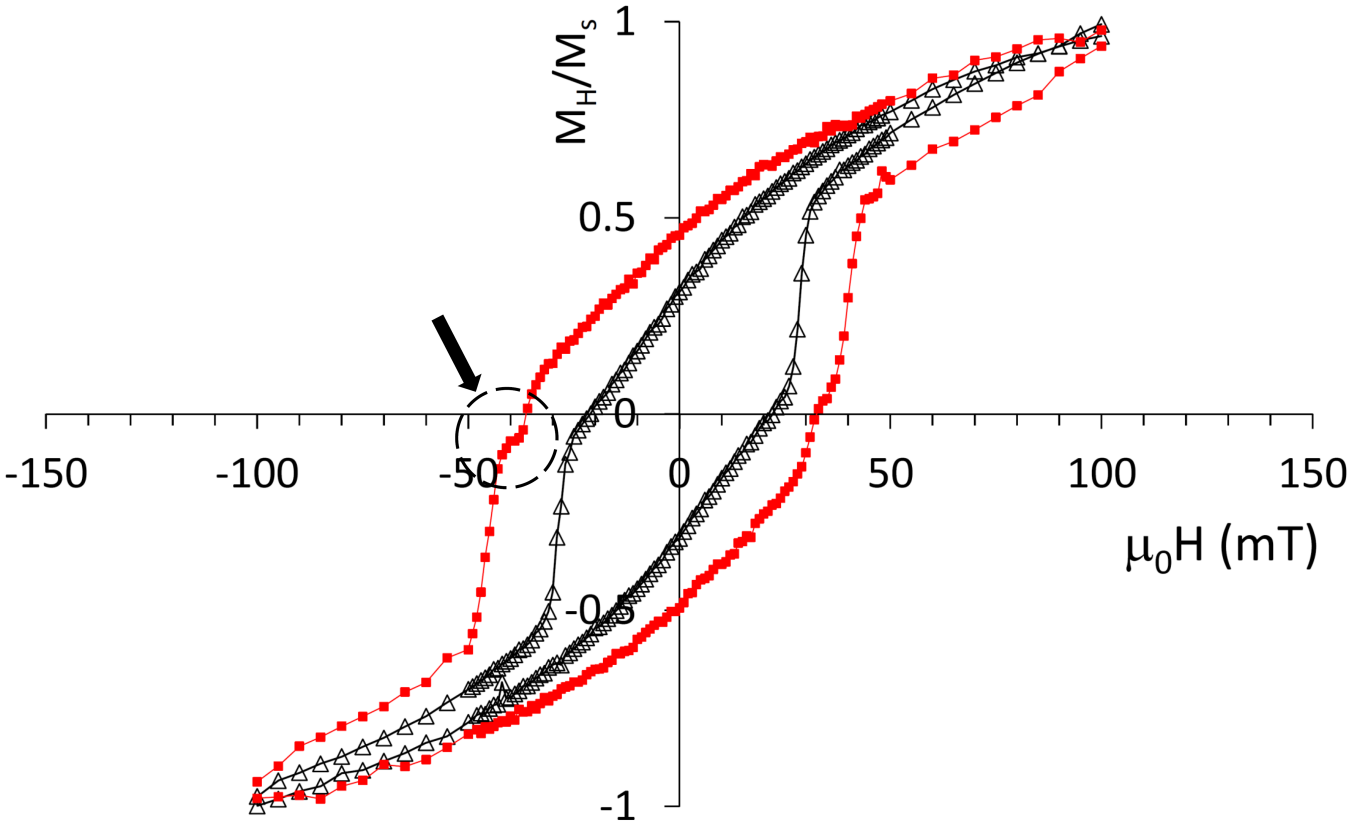
M_H/M_s
1
0.5
0
-0.5
-1
-150
-100
-50
0
50
100
150
μ_0H (mT)

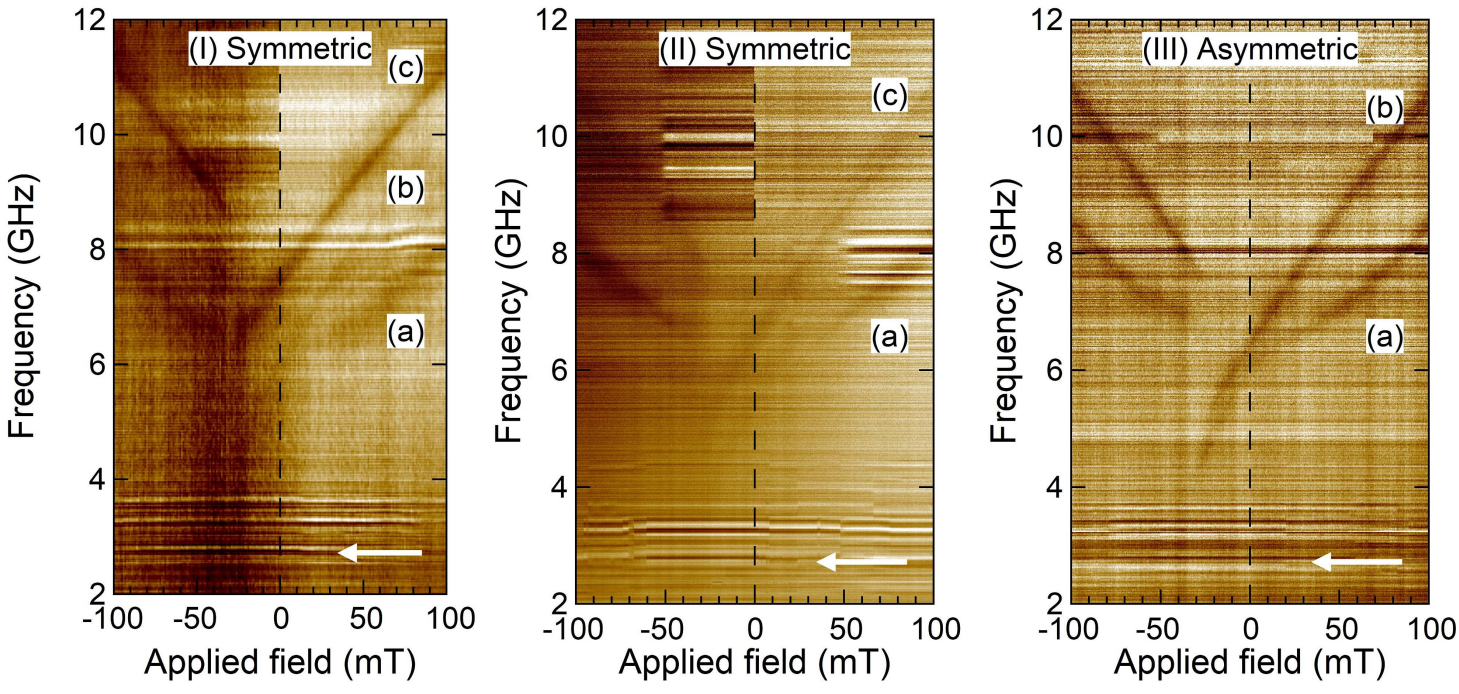
(I) Symmetric
(c)
(b)
(a)
(II) Symmetric
(c)
(a)
(III) Asymmetric
(b)
(a)
Frequency (GHz)
Applied field (mT)
12
10
8
6
4
2
-100
-50
0
50
100